POLITECNICO DI TORINO
Repository ISTITUZIONALE

Study of surface oxidation in metal powders by means of optical spectroscopy

Original
Study of surface oxidation in metal powders by means of optical spectroscopy / Giardino, M., Gobber, F.S., Pennacchio, A., Lupi, G., Casati, R., Actis Grande, M.. - In: POWDER TECHNOLOGY. - ISSN 0032-5910. - ELETTRONICO. - 443:(2024). [10.1016/j.powtec.2024.119883]

Availability:
This version is available at: 11583/2989211 since: 2024-06-02T05:32:56Z

Publisher:
Elsevier

Published
DOI:10.1016/j.powtec.2024.119883

Terms of use:

This article is made available under terms and conditions as specified in the corresponding bibliographic description in the repository

Publisher copyright

(Article begins on next page)

28 November 2026

Powder Technology 443 (2024) 119883

Contents lists available at ScienceDirect

Powder Technology

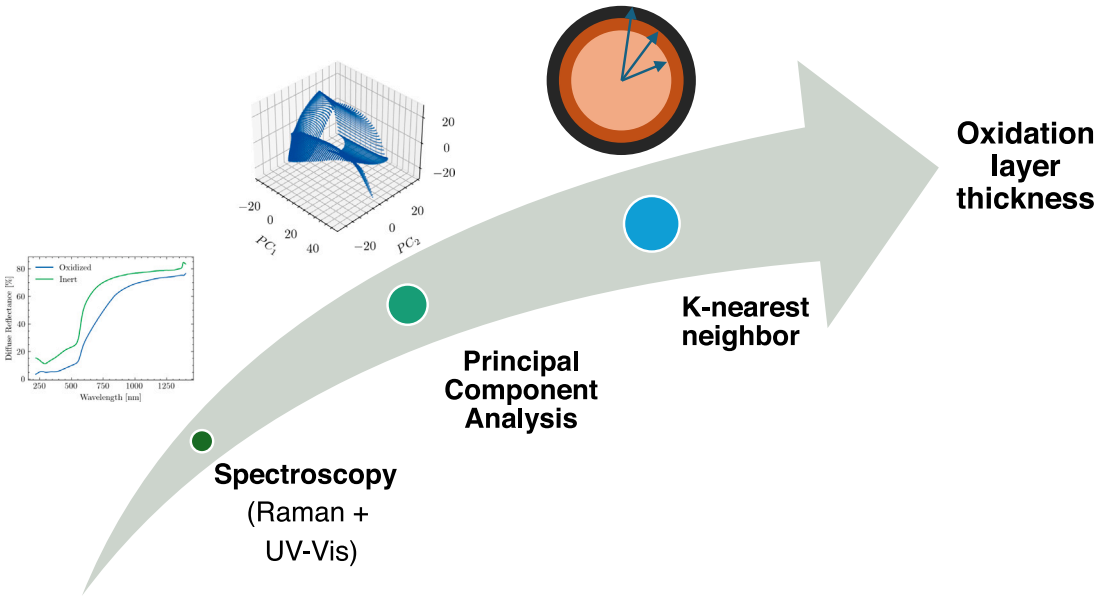
journal homepage: www.journals.elsevier.com/powder-technology

Study of surface oxidation in metal powders by means of optical spectroscopy

Matteo Giardino [a,b,*], Federico Simone Gobber [a,b], Antonio Pennacchio [a], Giorgia Lupi [c], Riccardo Casati [c], Marco Actis Grande [a,b]

[a] Department of Applied Science and Technology (DISAT), Politecnico di Torino, v. Teresa Michel 5, Alessandria, 15121, Alessandria, Italy
[b] National Interuniversity Consortium for Material Science and Technology (INSTM), v. G. Giusti 9, Firenze, 50121, Firenze, Italy
[c] Department of Mechanical Engineering, Politecnico di Milano, v. G. La Masa 34, Milan, 20156, Milan, Italy

GRAPHICAL ABSTRACT



HIGHLIGHTS

- The oxidation status on CuAg3.4 alloy powder is studied by optical spectroscopy.
- Raman spectroscopy allows the identification of the oxide composition.
- UV–Vis spectroscopy offers a method to ascertain the thickness of the oxide layer.

ARTICLE INFO

Keywords:
Metal powders
Oxidation layer

ABSTRACT

Copper alloy powders undergo oxidation upon exposure to ambient air conditions, leading to the formation of a metastable surface layer predominantly comprised of cuprous oxide (Cu_2O), which subsequently transitions to cupric oxide (CuO). Accurately quantifying the thickness of this oxide layer, typically spanning a few

* Corresponding author at: Department of Applied Science and Technology (DISAT), Politecnico di Torino, v. Teresa Michel 5, Alessandria, 15121, Alessandria, Italy.
E-mail address: matteo.giardino@polito.it (M. Giardino).

https://doi.org/10.1016/j.powtec.2024.119883
Received 31 March 2024; Received in revised form 8 May 2024; Accepted 17 May 2024
Available online 21 May 2024
0032-5910/© 2024 The Author(s). Published by Elsevier B.V. This is an open access article under the CC BY license (http://creativecommons.org/licenses/by/4.0/).

Raman spectroscopy
UV–Vis spectroscopy

nanometers, presents inherent challenges. This research delves into examining the composition and extent of the surface oxide layer on CuAg3.4 alloy powder, produced via gas atomization, utilizing Raman and UV–Vis spectroscopy. The primary objective of the investigation is to introduce a straightforward and innovative approach for evaluating the oxidation status of metal powders. Specifically, the composition of the oxide layer is assessed through Raman spectroscopy, whereas its thickness is determined through UV–Vis spectroscopy using a nearest-neighbor regression model trained on simulated spectra obtained by Mie's model. Furthermore, the study reveals the limitations of X-ray diffraction measurements in providing compositional insights into the oxide layer.

1. Introduction

Cu–Ag alloys are highly valued for the exceptional combination of high strength and high conductivity properties. The alloys have garnered significant attention across multiple industries, including electronic power, materials, machinery and in the field of high-field magnets [1,2]. Cu–Ag alloys' attributes make it an excellent choice for the preparation of magnetic coils, which are crucial components in numerous electrical and electronic applications [3]. Compared to other alloying elements, Ag shows a lower influence on the conductivity of copper alloys [4–6].

The microstructures and properties of the Cu–Ag systems are significantly influenced by several factors, including the Ag content, the heat treatment applied, and eventual plastic deformation. Among these factors, the Ag content plays a crucial role in determining the morphology, distribution, and precipitate of the Ag-rich phase within the alloy [7,8]. In order to concurrently improve the mechanical properties of Cu–Ag alloys while maintaining low cost and high electrical conductivity, low Ag contents have been investigated [9], with the addition of small amounts of Cr into the alloy.

Powder metallurgy techniques are distinguished by a high degree of microstructural cleanliness and homogeneity, rendering them well-suited for the fabrication of components with excellent electrical conductivity. Additive manufacturing (AM) represents the most recently developed branch of powder metallurgical techniques, and in recent years has garnered significant interest in research due to the high degree of design freedom it allows. In the context of Laser Powder Bed Fusion (L-PBF) or Direct Energy Deposition (DED), the laser-powder optical interaction, in conjunction with the metallurgical aspects related to solidification, plays a major role in determining the processability of powders.

Inappropriate storage conditions for AM metal powder feedstock can result in detrimental effects on both the powder itself and the final AM components produced. A study on the effect of the storage on powders characteristics and on the final properties of the Laser Powder Bed Fusion (LPBF) component is reported in [10], whereas in [11] some guidelines about powder storage and handling are reported.

Many powder manufacturers recommend storing Cu and Cu alloy powders in sealed containers, preferably in a dry and inert atmosphere such as argon [12]. However, for several reasons, powders may be accidentally exposed to the environment, with a strong risk of degradation of the material [13].

1.1. Oxide formation on copper powders

Cu powder oxidation was observed in several works focused on its surface characterization by means of a Focus Ion Beam (FIB) and X-ray photoelectron spectroscopy (XPS) [14]. In particular, Zhidovinova et al. [15] used XPS to investigate the powder oxidation state during the storage in standard environmental conditions. They observed that a cuprous oxide Cu_2O layer is rapidly formed on the surface of unoxidized copper powder particles. Such an oxide spontaneously transforms into a cupric oxide CuO during storage if no inert atmosphere is provided. However, this kind of study requires expensive instrumentation and entails complex and time-consuming sample preparation procedures. Additionally, particle sectioning by means of FIB processing may require extra precautions to avoid beam-induced reduction of the oxide layer [16,17].

As far as copper is concerned, it was observed that powders react with oxygen forming three different known oxide stoichiometry, namely CuO, Cu_2O and Cu_4O_3. The first two are stable forms whereas, Cu_4O_3 is a metastable form of little interest [18]. Both CuO and Cu_2O are p-type semiconductors that show a transition at 1.3–2.0 eV (direct) and 2.0–2.7 eV (indirect) respectively. However, in literature much higher gap energy are reported for CuO due to quantum confinement phenomena. This effect is usually negligible for Cu_2O being its Bohr exciton radius equal to 0.7 nm. The optical response of a spherical particle can be studied employing the Mie's theory. Gustav Mie [19] studied the problem of light scattering by a spherical particle using a multipole expansion of the electric and magnetic field and imposing appropriate boundary conditions at the particle-surrounding interface. According to Mie's scattering theory [20], the scattering cross-section σ_{sca} of a spherical particle of diameter d is given as follows:

$$\sigma_{sca} = \frac{2\pi}{|\mathbf{k}|^2} \sum_{l=1}^{\infty} (2l+1)\left(|a_l|^2 + |b_l|^2\right) \tag{1}$$

where $\mathbf{k}$ is the wave vector and the coefficients a_l and b_l are given respectively as described in (2) and (3).

$$a_l = \frac{m\psi_l(mx)\psi_l'(x) - \psi_l'(mx)\psi_l(x)}{m\psi_l(mx)\eta_l'(x) - \psi_l(mx)\eta_l(x)} \tag{2}$$

$$b_l = \frac{\psi_l(mx)\psi_l'(x) - m\psi_l'(mx)\psi_l(x)}{\psi_l(mx)\eta_l'(x) - m\psi_l(mx)\eta_l(x)} \tag{3}$$

A further generalization of this theory was introduced for the calculation of the scattering cross-section on a multilayered sphere [21,22]. In this case, the adopted approach is identical to the spherical particle, but a separate description for the fields in each layer together with boundary conditions at each interface is required. The present paper investigates the possibility of studying the surface oxidation of a CuAg3.4 metal powder produced by gas atomization, by means of optical spectroscopy. Raman spectroscopy is used to obtain compositional information [18] whereas UV–visible (UV–Vis) spectroscopy [19], coupled to a machine-learning algorithm, allows for the quantification of the thickness of the particle surface oxide layer.

2. Materials and methods

2.1. Powder fabrication

Cu3.4%Ag powders were produced using a vacuum induction inert gas atomizer (VIGA). Pure electrolytic Cu (99.99%) and pure Ag granules (99.9%) were placed in an alumina crucible in the proper amount and then heated up to reach a metal molten bath, under a high purity 5.0 Ar shielding gas cover at an overpressure of 0.05 barg. The molten bath was held at a stable temperature of 1255 ± 5 °C for 15 min. The overpressure in the melting chamber was then increased to 0.22 barg, and the melt was atomized with Ar at 42 bar. A gas-to-metal ratio of 1.35 was calculated as characteristic of the process. The amount of oxygen in the atomization chamber was monitored throughout the entire powder production process, using a Zircona probe sensor (Rapidox 1100). The oxygen content ranged from 0.005%wt immediately after atomization to 0.009%wt before unloading the gas-atomized powders.

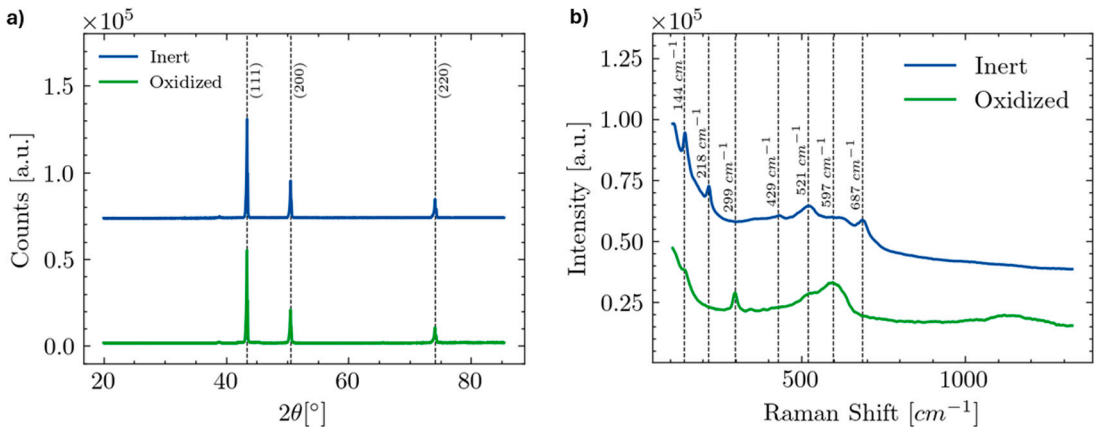


Fig. 1. X-ray diffraction spectra (a) and Raman spectra (b) for the two powder samples.

2.2. Sample preparation and characterization

Two batches of powder were produced and stored under different conditions: the first batch (oxidized) was stored at standard room conditions, whereas the second one (inert) was stored under a dry argon atmosphere, using silica bag as desiccant. All the powders were sieved to achieve a particle size distribution (PSD) of 20–63 μm, suitable for the LPBF process. A laboratory sieve shaker was used with three 200 mm diameter sieves (20 μm, 63 μm, and 120 μm), and 0.5 kg of powder was added for each run. Volume size distributions were measured using a Malvern Panalytical MasterSizer 3000 laser diffraction particle analyzer. The oxygen content of the powder was measured using the inert gas fusion technique (Leco ONH 836). The X-ray diffraction (XRD) spectra were collected in a Malvern Panalytical Empyrean X-ray diffractometer using a zero-background powder holder. Spectra were acquired in the 2θ range from 20° to 90°, with a step size of 0.013°.

Powders were fixed onto an aluminum stub using a double-side carbon tape and their Raman spectra were collected in an inVia Renishaw Raman confocal microscope equipped with a 50x (NA = 0.75) objective. A 633 nm laser at a power of 1.7 mW was used as the excitation source. Spectra were collected after an exposure of 6 s and 4 accumulations. The same samples were imaged without further preparation in Zeiss Supra 40 Field Emission Scanning Electron Microscope (FESEM) operated at 300 V or 5 kV, using the InLens detector. Compositional information was obtained through Energy Dispersion Spectroscopy (EDS) operating the instrument at 6 kV and 20 kV (see Supporting Information). The alloy microstructure was observed after etching the cross-sectioned powder, embedded in conductive epoxy resin, for 6 s in an ammonium persulfate $0.4M$ solution and collecting the image using the backscattered electron detector (BSD) in compositional contrast mode.

Diffuse reflectance $\%R$ spectra at normal incidence (0°) were recorded using a Shimadzu UV2600i spectrophotometer equipped with an ISR2600 plus integration sphere in the wavelength range from 300 nm to 1000 nm with a wavelength step of 0.2 nm. Absorption coefficient F_{kbm} were calculated according to Kubelka–Munk theory [23] as follows:

$$F_{kbm} = \frac{(1 - \frac{\%R}{100})^2}{2\frac{\%R}{100}} \tag{4}$$

2.3. Optical response simulation

Optical data for Cu and Ag were taken from Johnson–Christy [24]. Optical data for CuO and Cu_2O and AgO were taken from Palik [25]. Dielectric function ε_{Br} for composite layers were calculated via effective medium theory approach using Bruggeman's formula [26]:

$$\varepsilon_{Br} = \frac{1}{4}\left(\beta + i\sqrt{-\beta^2 - 8\varepsilon_A\varepsilon_B}\right) \tag{5}$$

where ε_A and ε_B are the dielectric functions of the components A and B and β is given as:

$$\beta = (2 - 3\phi_B)\varepsilon_A + (1 - 3\phi_B)\varepsilon_B \tag{6}$$

where ϕ_B is the volume fraction of the component B.

The optical response of spherical particles, whose structure is shown in Fig. 5, was simulated using the Mie scattering theory implemented in the *scattnlay* [21,22] Python library. Being the particle size much bigger than the incident wavelength (300 – 1000 nm), simulations were performed using a multiple-precision representation.

2.4. Calculation of the oxide layer thickness via k-nearest neighbor regression

Reflectance in experimental UV–Vis spectra R_{exp} was normalized from 0 to 1 to obtain a normalized experimental reflectance $\hat{R}_{exp}$. Also scattering cross sections σ_{sca} obtained from simulations was normalized to obtain a normalized simulated reflectance $\hat{R}_{sim}$. Subsequently, principal component analysis (PCA) was applied to transform the simulated spectra into a reduced-dimensional space with five components using the Scikit-learn Python library [27]. Experimental spectra were projected into the principal component space using the previously trained model. Employing k-nearest neighbor regression, with 25 neighbors, the thickness of the oxide layers was determined based on the transformed spectra. The goodness of the fitting was quantified by calculating the mean square error χ_{fit} between the experimental spectra and its nearest neighbor (best fit).

$$\chi_{fit} = \frac{1}{N}\sqrt{\sum^{\lambda}[\hat{R}_{exp}(\lambda) - \hat{R}_{sim}(\lambda)]^2} \tag{7}$$

3. Results and discussion

Two CuAg3.4 powder batches were produced by gas atomization and stored under different conditions for 1 month. One batch was stored under room condition (oxidized), whereas was stored under inert Ar gas, and silica gel bags were added to prevent moisture absorption and oxidation (inert). The purpose of the present work was to investigate the application of a spectroscopy-based approach for the study of the surface oxidation state of the two powder batches. SEM images of the two powder batches collected after the atomization are reported in Figure S1, demonstrating the high sphericity of the particles. The oxygen content was measured immediately after the atomization using the inert gas fusion technique (Leco ONH 836) resulting in a value of 0.024 ± 0.002%wt. and 0.044 ± 0.003%wt. for the inert and oxidized samples respectively. Size distributions were determined by means of laser granulometry returning an average diameter equal to 39.7 μm for the oxidized sample and to 43.2 μm for the inert sample (see Figure

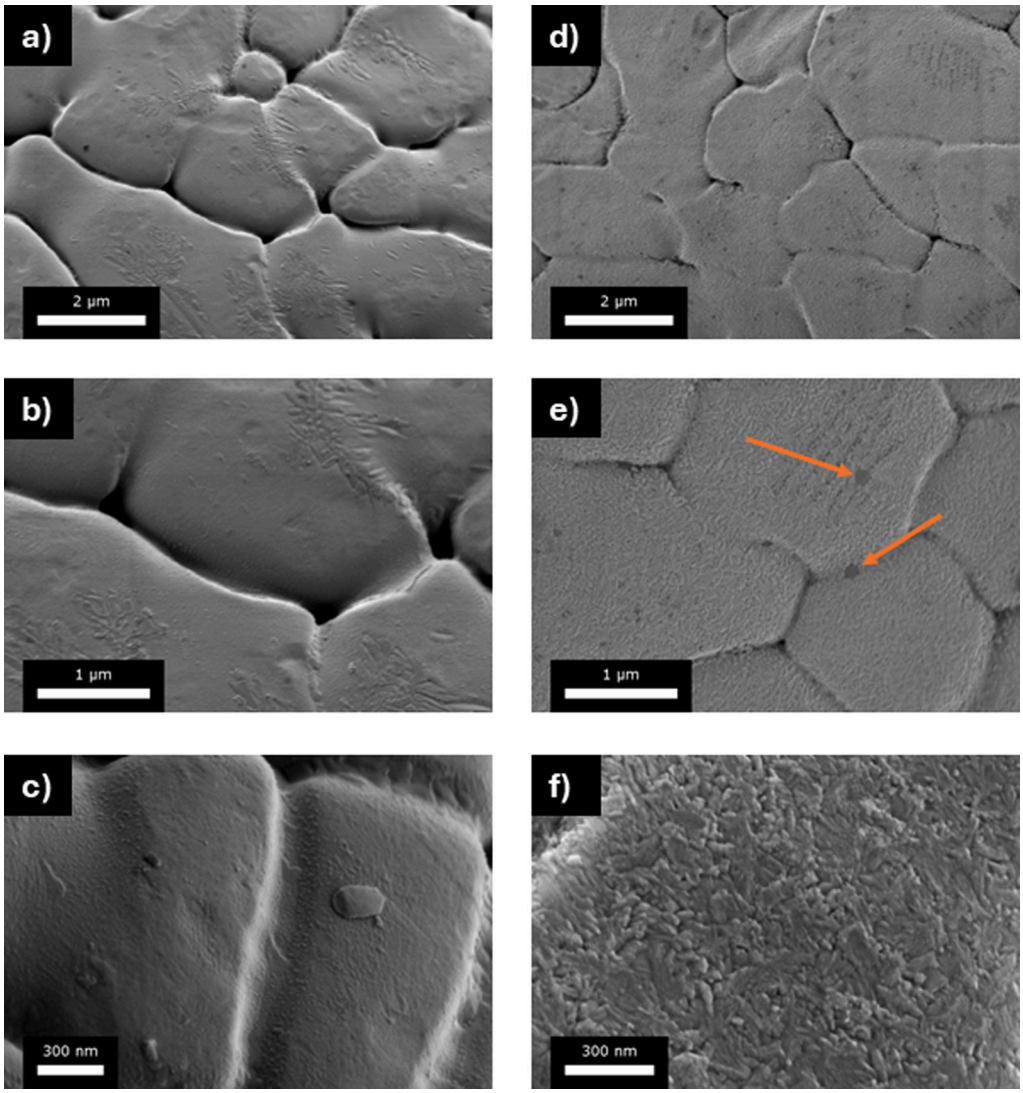


Fig. 2. FESEM images of the particle surface for the inert (a–c) and oxidized powder (d–f). In the picture (e) the holes in the oxide layers are marked with orange arrows.

S2). The X-ray diffractograms, reported in Fig. 1(a), show the same diffraction pattern for both the two samples. In fact, the diffraction peaks, located at 43.43°, 50.53° and 73.35° are associated to the (111), (200) and (220) planes of face-centered cubic (fcc) copper respectively. The peaks associated to Cu_2O and CuO are not observed suggesting that the oxide layers are not thick enough to give any significant signal contribution in Bragg–Brentano geometry. For this reason, we conclude that XRD does not provide information on the composition of the particles outer layer and it is not suitable for this kind of investigation. The Raman spectra of the powders were collected using a Raman confocal microscope as described in the Method section. They show strong bands due to the presence of different copper and silver oxides as reported in Table 1. In particular, the oxidized powder exhibits the two bands of CuO [28], i.e. 299 cm^{-1} and 597 cm^{-1}. On the other hand, the inert sample also shows Cu_2O bands [28,29] located at 144 cm^{-1} and 218 cm^{-1}. Inert sample spectra exhibits a band at 678 cm^{-1} which is probably attributed to the presence of Ag_2O [30].

Micrographs of the powder captured at the FESEM are reported in Fig. 2. Such measurements were performed operating the FESEM in low voltage mode at 300 V to reduce the interaction volume. In fact, at lower energy levels, the electron beam penetrates only a few tens of nanometers. Consequently, the resultant image solely encompasses details pertaining to the surface and the adjacent near-surface regions of the specimen. High magnifications micrographs reported in Fig. 2 (c) and (f) were able to show the difference in the surface features between the inert and oxidized samples. The inert sample displayed a smooth surface, whereas the oxidized sample exhibited discernible roughness. Notably, the oxidized layer displayed distinctive holes, suggesting a wrapping-like morphology. The microstructure of the powder was observed at the FESEM using the BSD detector in compositional contrast mode after a microstructural etching using ammonium persulfate as indicated in the E407 ASTM standard [31]. EDS quantification (see Fig. 4) performed at 20 kV confirmed the composition of the alloy giving a content of silver equal to 3.3%wt. and 3.4%wt. in the inert and oxidized samples respectively. Spectra collected at low voltage, i.e. 6 kV, were able to sense the difference in the oxygen content returning an oxygen content of 5.6%wt. and 8.9%wt. As revealed in Fig. 3 (a) and in

Table 1
Assignment of the Raman band observed in the spectra reported in Fig. 1(b).

Band number	Raman shift [cm^{-1}]	Compound
1	144	Cu_2O
2	218	Cu_2O
3	299	CuOAg
4	429	AgO
5	521	Cu_2O
6	597	CuO
7	687	Ag_2O

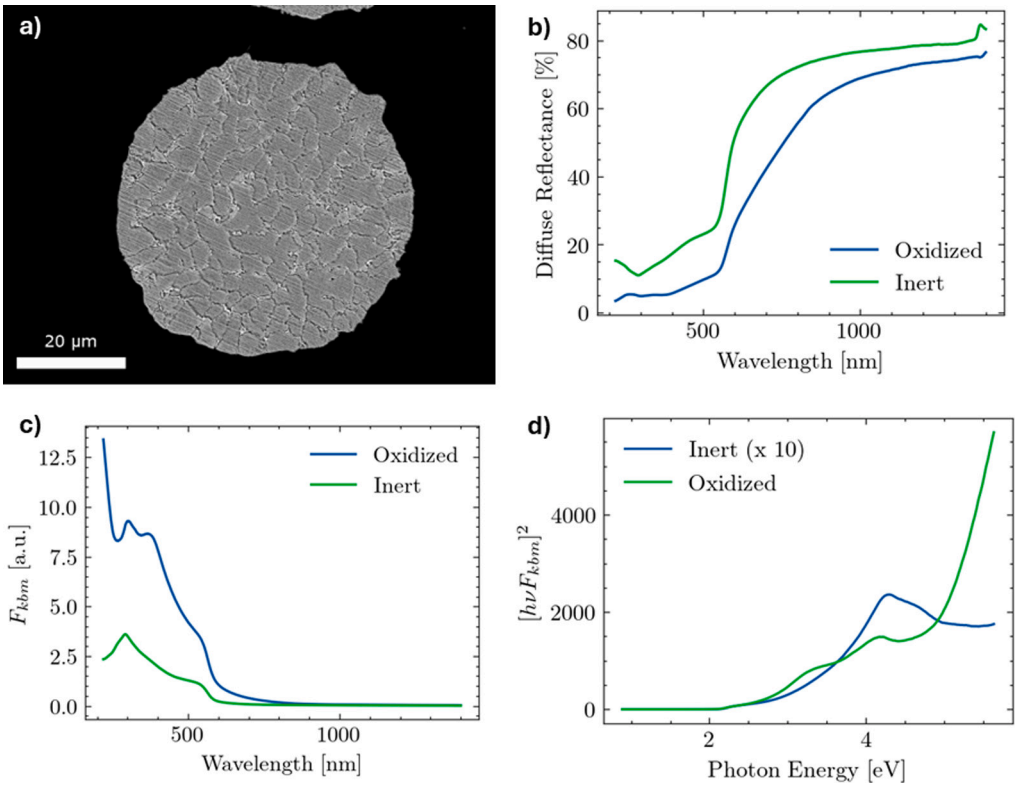


Fig. 3. Micrograph of the cross-sectioned powder after a microetching attack with the ammonium persulfate (a). Reflectance spectra (b), Kubelka–Munk plot (c) and Tauc plot (d) for the powder samples.

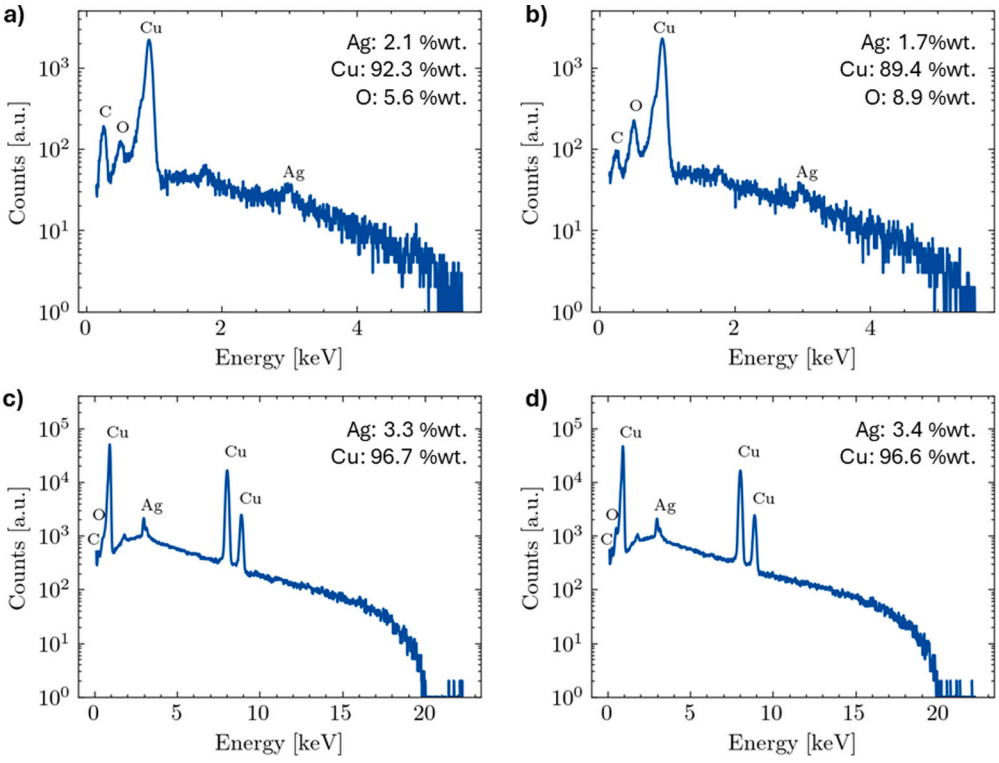


Fig. 4. EDS spectra collected at 6 kV on the inert (a) and oxidized (b) samples. EDS collected on the same samples at 20 kV (c and d).

the EDS mapping (Fig. S3), the powder microstructure is characterized by fine dendrites with Ag-enriched segregations in the interdendritic arms, which is consistent with the rapid solidification mechanism. After the Cu–Ag equilibrium phase diagram, the Cu-rich α-phase nucleates at high temperature directly from the liquid phase, with the Ag-rich β-phase precipitating at the solid state. In light of this, we assume

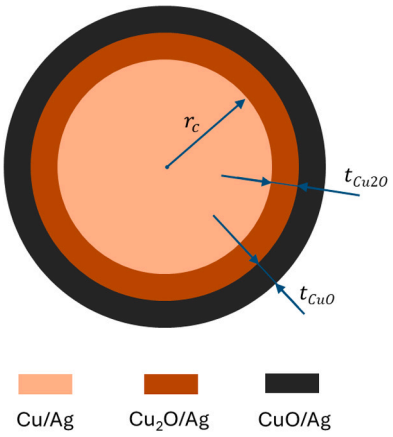


Fig. 5. Representation of the assumed layered structure for a single powder particle.

that the disperse phase (Ag) exhibits long-range connectivity and that Bruggeman's [32] hypothesis are fulfilled.

UV–Vis spectra shown in Fig. 3 (b) report a significant difference in the optical response of the two samples. The oxidized sample demonstrates a lower reflectance in the whole considered spectral range. However, due to the composite nature of the particles, it is not possible to identify the two oxides according to their different bandgap energy from Tauc plots (Fig. 3d).

A particle model was created to calculate the optical response by means of simulation. It was assumed that a powder particle is made up of a Cu core a radius r_c, a Cu_2O layer of thickness t_{Cu_2O} and a CuO layer of thickness t_{CuO} as shown in Fig. 5. The total radius of the particle is $r_{tot} = r_c + t_{CuO} + t_{Cu_2O}$. Considering the Cu–Ag phase diagram, it is assumed that the powder is initially composed of a pure Cu phase and a pure Ag phase. The volume fraction of the Ag phase ϕ_{Ag}^{Cu} in Cu layer was calculated to be 2.9%wt. Following the same idea, the volume fraction of the Ag phase in the Cu_2O and CuO layer was calculated to be equal to $\phi_{Ag}^{Cu_2O} = 1.7\%$ and $\phi_{Ag}^{CuO} = 1.6\%$. The optical properties with these compositions were calculated using an effective medium theory approach as described in the Method section by Bruggeman's formula [32–34] and are reported in Fig. 6a–c. However, as reported in several works, the actual refractive index of a thin film can be different from the one of the bulk material due to quantum confinement [35,36]. In fact, like all semiconductors, also copper oxide films exhibit a dependence of the optical properties on the film thickness as it moves to the nanometer scale, due to a quantum confinement mechanism that leads to the splitting of both the valence and conduction band into discrete levels. This phenomenon is relevant for the film whose thickness is equal to or lower than the Bohr exciton radius r_B which, in this case, is equal to $6.6 - 28.7$ nm [37], and 0.7 nm [38] in CuO and Cu_2O respectively. This phenomenon is likely to be negligible for the Cu_2O layer whereas it may be important for the CuO layer, however, no detailed models for such a correction have been developed so far and the effect is neglected within the frame of this paper.

Optical data for the Cu/Ag,Cu_2O/Ag and CuO/Ag layers were calculated using the Bruggeman's effective medium theory and are reported in Fig. 6.

Different spectra for a particle with a total radius r_{tot} and with different values of layer thickness t_{Cu_2O} and t_{CuO} in the range from 0 to 50 nm were calculated using the Mie's models implemented in the *scattnlay* library. The obtained spectra were transformed into their principal component system using a number of principal components equal to 5 to achieve an explained variance greater than 95% as shown in Fig. 7 (a). The representation of the simulated spectra in the space of the first three principal components, namely P.C. 1, P.C. 2 and P.C. 3, is reported in 7 (b). The thickness of the oxide layers t_{Cu_2O} and t_{CuO} on the two samples were calculated by classifying the experimental spectra using a k-nearest neighbor regression model trained on the simulated data. Experimental spectra together with their respective nearest neighbor (best fit) are reported in Fig. 7 (c) and (d). The thicknesses of the oxide layers derived from the k-nearest neighbor regression are presented in Table 2 and are consistent with the composition discerned via Raman spectroscopy. Specifically, our analysis reveals that inert specimens exhibit analogous thicknesses of CuO and Cu_2O, while in the oxidized sample, the oxide layer is predominantly constituted by CuO (13.9 nm).

Table 2
Thickness of the oxide layers resulted from the k-nearest neighbor regression.

Sample	r_c [μm]	t_{Cu_2O} [nm]	t_{CuO} [nm]	χ_{fit}
Oxidized	19.5	1.4	13.9	$2.15 \cdot 10^{-2}$
Inert	21.5	2.1	3.3	$2.83 \cdot 10^{-2}$

4. Conclusion

The CuAg3.4 alloy powder, produced via gas atomization and subjected to varying storage conditions, underwent comprehensive characterization utilizing Raman and UV–Vis spectroscopy. The primary objective was to quantify the thickness of the surface layer resulting from metal oxidation. Raman spectroscopy revealed that the inert sample predominantly comprised cuprous oxide, whereas the oxidized sample exhibited a higher quantity of cupric oxide. This finding aligns with existing literature documenting the spontaneous transition from Cu_2O to CuO during storage under ambient air conditions. Subsequently, a nearest-neighbor regression model was developed using scattering spectra derived from simulated layered particles via the Mie model. This model was then applied to analyze the experimental UV–Vis spectra obtained from both powder samples to estimate the thickness of the surface oxide layers. The proposed technique is therefore a simple and easy-to-use tool to study the oxidation state of copper alloy powder and represents an effective alternative to more complex techniques such as XPS and FIB when a rough estimation is required.

CRediT authorship contribution statement

Matteo Giardino: Writing – review & editing, Writing – original draft, Visualization, Validation, Software, Methodology, Investigation, Data curation, Conceptualization. **Federico Simone Gobber:** Methodology, Investigation. **Antonio Pennacchio:** Methodology, Investigation. **Giorgia Lupi:** Conceptualization. **Riccardo Casati:** Conceptualization. **Marco Actis Grande:** Writing – review & editing, Visualization, Supervision, Project administration, Methodology, Funding acquisition, Conceptualization.

Declaration of competing interest

The authors declare that they have no known competing financial interests or personal relationships that could have appeared to influence the work reported in this paper.

Data availability

Data will be made available on request.

Appendix A. Supplementary data

Supplementary material related to this article can be found online at https://doi.org/10.1016/j.powtec.2024.119883.

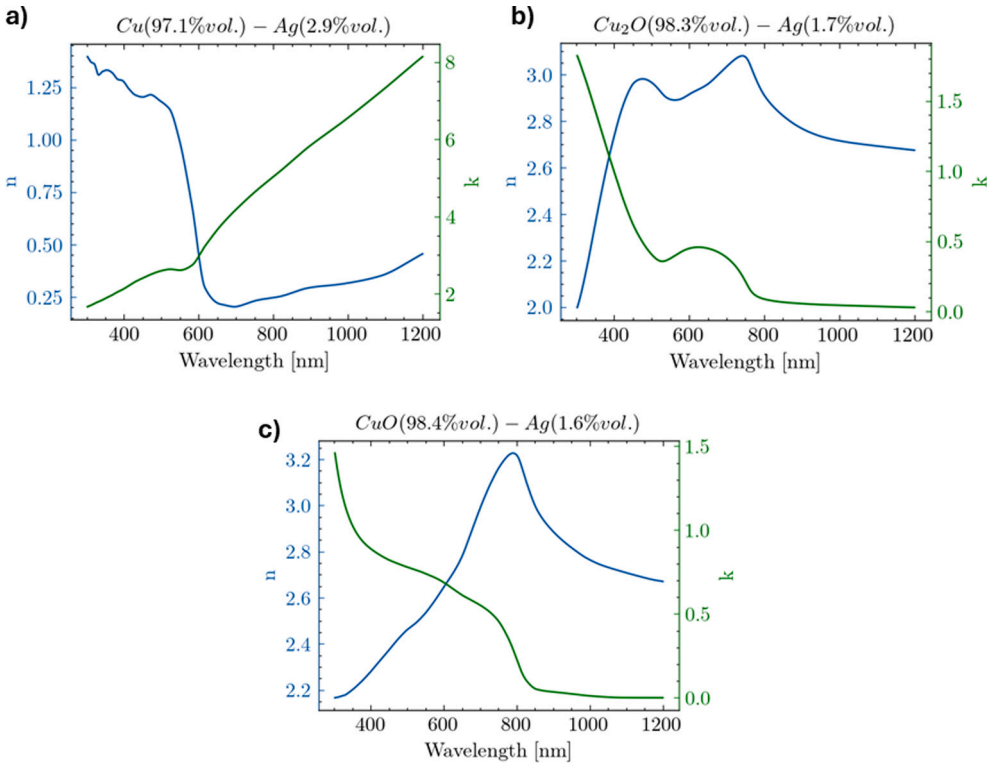


Fig. 6. Optical data for the Cu/Ag (a), Cu_2O/Ag (b) and CuO/Ag (c) layers calculated using the Bruggeman's effective medium theory.

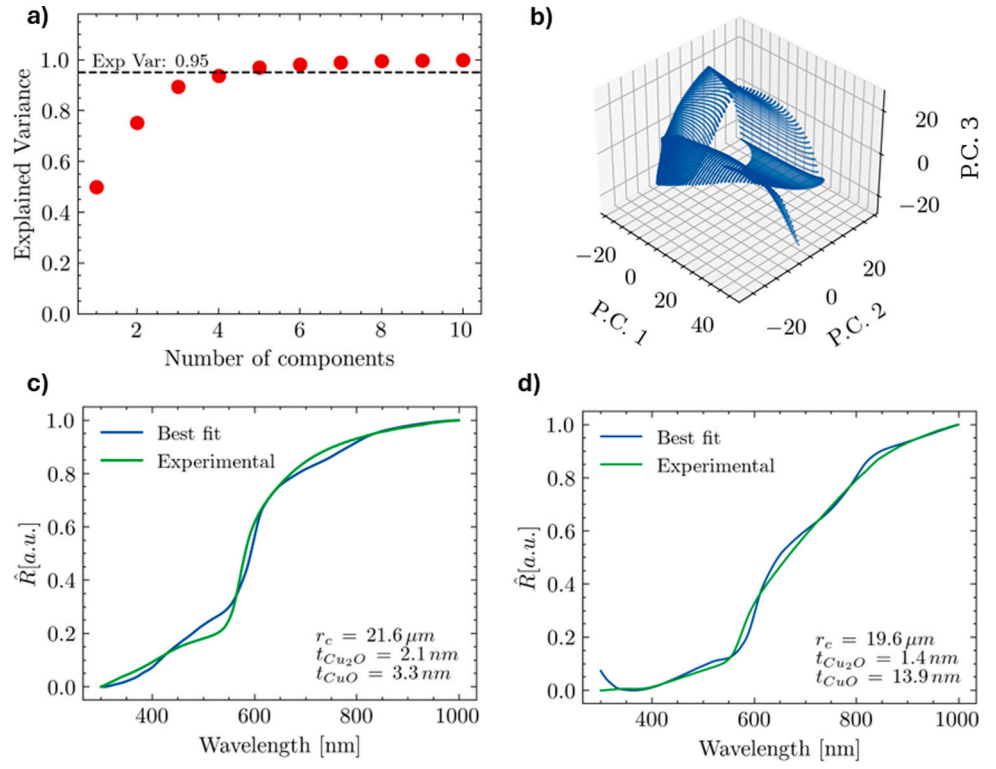


Fig. 7. (a) Explained variance as a function of the PCA component number. (b) Representation of the simulated spectra in the principal component coordinate system. Results of the k-nearest neighbor regression for the inert (c) and oxidized (d) powder sample.

References

[1] C. Zhao, R. Niu, Y. Xin, D. Brown, D. McGuire, E. Wang, K. Han, Improvement of properties in Cu–Ag composites by doping induced microstructural refinement, Mater. Sci. Eng. A 799 (2021) 140091, http://dx.doi.org/10.1016/j.msea.2020.140091.

[2] M. Xie, W. Huang, H. Chen, L. Gong, W. Xie, H. Wang, B. Yang, Microstructural evolution and strengthening mechanisms in cold-rolled Cu–Ag alloys, J. Alloys Compd. 851 (2021) 156893, http://dx.doi.org/10.1016/j.jallcom.2020.156893.

[3] G. Bao, Y. Xu, L. Huang, X. Lu, L. Zhang, Y. Fang, L. Meng, J. Liu, Strengthening effect of Ag precipitates in Cu–Ag alloys: A quantitative approach, Mater. Res. Lett. 4 (1) (2016) 37–42, http://dx.doi.org/10.1080/21663831.2015.1091795.

[4] Y. Sakai, K. Inoue, T. Asano, H. Wada, H. Maeda, Development of high-strength, high-conductivity Cu–Ag alloys for high-field pulsed magnet use, Appl. Phys. Lett. 59 (23) (1991) 2965–2967, http://dx.doi.org/10.1063/1.105813.

[5] H. Yang, Z. Ma, C. Lei, L. Meng, Y. Fang, J. Liu, H. Wang, High strength and high conductivity Cu alloys: A review, Sci. China Technol. Sci. 63 (12) (2020) 2505–2517, http://dx.doi.org/10.1007/s11431-020-1633-8.

[6] X. Zhu, Z. Xiao, J. An, H. Jiang, Y. Jiang, Z. Li, Microstructure and properties of Cu-Ag alloy prepared by continuously directional solidification, J. Alloys Compd. 883 (2021) 160769, http://dx.doi.org/10.1016/j.jallcom.2021.160769.

[7] C. Zhao, X. Zuo, E. Wang, R. Niu, K. Han, Simultaneously increasing strength and electrical conductivity in nanostructured Cu–Ag composite, Mater. Sci. Eng. A 652 (2016) 296–304, http://dx.doi.org/10.1016/j.msea.2015.11.067.

[8] C. Zhao, X. Zuo, E. Wang, K. Han, Strength of Cu-28 wt%Ag composite solidified under high magnetic field followed by cold drawing, Met. Mater. Int. 23 (2) (2017) 369–377, http://dx.doi.org/10.1007/s12540-017-6417-2.

[9] X. Guo, L. Zhang, D. Zhang, X. Zhao, Y. Zhang, E. Wang, Enhanced precipitation-hardening of Cu-Ag alloys through controlled chromium addition, Mater. Lett. 357 (2024) 135815, http://dx.doi.org/10.1016/j.matlet.2023.135815.

[10] K. Riener, S. Oswald, M. Winkler, G.J. Leichtfried, Influence of storage conditions and reconditioning of AlSi10Mg powder on the quality of parts produced by laser powder bed fusion (LPBF), Addit. Manuf. 39 (2021) 101896, http://dx.doi.org/10.1016/j.addma.2021.101896.

[11] S. Hall, A. Chrostek-Mroz, J. Dawes, Developing storage and handling guidelines for additive manufacturing metal powder feedstock, in: Progress in Additive Manufacturing 2020, ASTM International, 2022, pp. 1–12, http://dx.doi.org/10.1520/STP163720210005.

[12] Copper Powder - ESPI Metals, URL https://www.espimetals.com.

[13] J. Grubbs, B.C. Sousa, D. Cote, Exploration of the effects of metallic powder handling and storage conditions on flowability and moisture content for additive manufacturing applications, Metals 12 (4) (2022) 603, http://dx.doi.org/10.3390/met12040603.

[14] M.M. Mahmoud, Characterization of the native oxide shell of copper metal powder spherical particles, Materials 15 (20) (2022) 7236, http://dx.doi.org/10.3390/ma15207236.

[15] S.V. Zhidovinova, L.V. Zolotukhina, B.R. Gel'chinskii, Oxidation of copper ultrafine powders and nanopowders produced by vapor phase condensation, Russ. Metall. (Met.) 2010 (9) (2010) 774–778, http://dx.doi.org/10.1134/S0036029510090053.

[16] T. Kobayashi, F. Nishiyama, K. Takahiro, Chromatic change in copper oxide layers irradiated with low energy ions, Quantum Beam Sci. 5 (1) (2021) 7, http://dx.doi.org/10.3390/qubs5010007.

[17] N.J. Long, A.K. Petford-Long, In-situ electron-beam-induced reduction of CuO: A study of phase transformations in cupric oxide, Ultramicroscopy 20 (1) (1986) 151–159, http://dx.doi.org/10.1016/0304-3991(86)90181-6.

[18] M. Razavipour, S. Rahmati, A. Zúñiga, D. Criado, B. Jodoin, Bonding mechanisms in cold spray: Influence of surface oxidation during powder storage, J. Therm. Spray Technol. 30 (1) (2021) 304–323, http://dx.doi.org/10.1007/s11666-020-01123-5.

[19] G. Mie, Beiträge zur optik trüber medien, speziell kolloidaler metallösungen, Ann. Phys., Lpz. 330 (3) (1908) 377–445, http://dx.doi.org/10.1002/andp.19083300302.

[20] C.F. Bohren, D.R. Huffman, Absorption and Scattering of Light by Small Particles, John Wiley & Sons, 2008.

[21] K. Ladutenko, U. Pal, A. Rivera, O. Peña-Rodríguez, Mie calculation of electromagnetic near-field for a multilayered sphere, Comput. Phys. Comm. Complete (214) (2017) 225–230, http://dx.doi.org/10.1016/j.cpc.2017.01.017.

[22] O. Peña, U. Pal, Scattering of electromagnetic radiation by a multilayered sphere, Comput. Phys. Comm. 180 (11) (2009) 2348–2354, http://dx.doi.org/10.1016/j.cpc.2009.07.010.

[23] P. Makuła, M. Pacia, W. Macyk, How to correctly determine the band gap energy of modified semiconductor photocatalysts based on UV–vis spectra, J. Phys. Chem. Lett. 9 (23) (2018) 6814–6817, http://dx.doi.org/10.1021/acs.jpclett.8b02892.

[24] P.B. Johnson, R.W. Christy, Optical constants of the noble metals, Phys. Rev. B 6 (12) (1972) 4370–4379, http://dx.doi.org/10.1103/PhysRevB.6.4370, Publisher: American Physical Society.

[25] E.D. Palik, Handbook of Optical Constants of Solids, Academic Press, 1998.

[26] B.A. Belyaev, V.V. Tyurnev, Electrodynamic calculation of effective electromagnetic parameters of a dielectric medium with metallic nanoparticles of a given size, J. Exp. Theor. Phys. 127 (4) (2018) 608–619, http://dx.doi.org/10.1134/S1063776118100114.

[27] F. Pedregosa, G. Varoquaux, A. Gramfort, V. Michel, B. Thirion, O. Grisel, M. Blondel, P. Prettenhofer, R. Weiss, V. Dubourg, J. Vanderplas, A. Passos, D. Cournapeau, M. Brucher, M. Perrot, E. Duchesnay, Scikit-learn: Machine learning in python, J. Mach. Learn. Res. 12 (2011) 2825–2830.

[28] Y. Alajlani, F. Placido, A. Barlow, H.O. Chu, S. Song, S. Ur Rahman, R. De Bold, D. Gibson, Characterisation of Cu2O, Cu4O3, and CuO mixed phase thin films produced by microwave-activated reactive sputtering, Vacuum 144 (2017) 217–228, http://dx.doi.org/10.1016/j.vacuum.2017.08.005.

[29] H. Dizajghorbani Aghdam, S. Moemen Bellah, R. Malekfar, Surface-enhanced Raman scattering studies of Cu/Cu2O Core-shell NPs obtained by laser ablation, Spectrochim. Acta A 223 (2019) 117379, http://dx.doi.org/10.1016/j.saa.2019.117379.

[30] M. Yang, R. You, L. Dan, Z. Zhenhua, W. Huang, Methanol partial oxidation over shaped silver nanoparticles derived from cubic and octahedral Ag2O nanocrystals, Catal. Lett. 149 (2019) http://dx.doi.org/10.1007/s10562-019-02850-3.

[31] Standard practice for microetching metals and alloys, 2007, URL https://www.astm.org/e0407-07r15e01.html.

[32] T.C. Choy, Effective Medium Theory: Principles and Applications, Oxford University Press, 2016.

[33] D.A.G. Bruggeman, Berechnung verschiedener physikalischer konstanten von heterogenen Substanzen. I. Dielektrizitätskonstanten und leitfähigkeiten der mischkörper aus isotropen substanzen, Ann. Phys., Lpz. 416 (7) (1935) http://dx.doi.org/10.1002/andp.19354160705.

[34] W.R. Tinga, W.A.G. Voss, D.F. Blossey, Generalized approach to multiphase dielectric mixture theory, J. Appl. Phys. 44 (9) (1973) 3897–3902, http://dx.doi.org/10.1063/1.1662868.

[35] I.A. Starkov, A.S. Starkov, The thickness dependence of dielectric permittivity in thin films, J. Phys. Conf. Ser. 741 (1) (2016) 012004, http://dx.doi.org/10.1088/1742-6596/741/1/012004.

[36] M.Y. Lee, S.-H. Kim, I.-K. Park, Cu2O quantum dots emitting visible light grown by atomic layer deposition, Physica B 500 (2016) 4–8, http://dx.doi.org/10.1016/j.physb.2016.07.025.

[37] K. Borgohain, S. Mahamuni, Formation of single-phase CuO quantum particles, J. Mater. Res. 17 (2002) 1220–1223, http://dx.doi.org/10.1557/JMR.2002.0180.

[38] K. Karpinska, M. Mostovoy, M.A. van der Vegte, A. Revcolevschi, P.H.M. van Loosdrecht, Decay and coherence of two-photon excited yellow orthoexcitons in Cu2O, Phys. Rev. B (15) (2005) 155201.